AGU PUBLICATIONS

JGR

Journal of Geophysical Research: Solid Earth

RESEARCH ARTICLE
10.1002/2014JB011802

Key Points:
- Depressed MTZ marks a sharp craton-Cordillera transition in southern Alberta
- Depressed 410 with increased P410s amplitude imply partial melts above 410
- The cold slab fragments may cause a depressed 660 and thickened MTZ

Supporting Information:
- Figures S1 and S2

Correspondence to:
Y. J. Gu,
ygu@ualberta.ca

Citation:
Gu, Y. J., Y. Zhang, M. D. Sacchi, Y. Chen, and S. Contenti (2015), Sharp mantle transition from cratons to Cordillera in southwestern Canada, *J. Geophys. Res. Solid Earth*, *120*, doi:10.1002/2014JB011802.

Received 25 NOV 2014
Accepted 10 JUN 2015
Accepted article online 12 JUN 2015

Sharp mantle transition from cratons to Cordillera in southwestern Canada

Yu Jeffrey Gu[1], Yuanyin Zhang[1,2,3], Mauricio D. Sacchi[1], Yunfeng Chen[1], and Sean Contenti[1]

[1]Department of Physics, University of Alberta, Edmonton, Alberta, Canada, [2]Lab for the Integration of Geology and Geophysics, China University of Petroleum, Beijing, China, [3]Petroleum Exploration & Production Research Institute, SINOPEC, Beijing, China

Abstract The Western Canada Sedimentary Basin marks the transition from the old North American continental lithosphere to young accreted terranes. Earlier studies in this region have suggested a large number of intricate basement domains as well as major seismic velocity gradients in the mantle. To investigate the effect of the accretion and subduction on the mantle structure beneath the western margin of the North American Craton, we analyze *P*-to-*S* converted waves from upper mantle discontinuities from the Canadian Rockies and Alberta Network, a regional broadband seismic array based in Alberta, Canada. The depths of the 410 and 660 km seismic discontinuities are correlated and, on average, are 9 km and 7 km greater than their respective global estimates. The largest depression is observed beneath the Rocky Mountain foreland belt in southern Alberta, which highlights a steep southward/westward structural gradient from the cratons to Cordillera at lithospheric mantle depths. The severity of the depressions, especially in the southernmost Alberta, may be triggered by diffuse partial melt or increased water content above the 410 km discontinuity. This result is corroborated by locally increased impedance contrast across the 410 km discontinuity and a strongly depressed 660 km discontinuity. A relic Mesozoic slab fragment may be partially responsible for the deep olivine phase boundary at the base of the upper mantle.

1. Introduction

The North American continent, a very complex assemblage of disparate geological units, has undergone significant periods of deformation, faulting, rifting, and accretion throughout its history. The ancient core of the continent, which consists of a number of Archean provinces, is among the oldest continental cratons in the world. Its origin remains speculative, though the existing geological and geophysical evidence has generally implicated the coeval assembly of the Hearne, Superior, Rae, Slave, and Wyoming provinces [*Hoffman*, 1988; *Ross et al*., 1991] approximately 2.0 Gyr ago. Following the collision of these former "microcontinents" to form the ancestral core, the North American continent was expanded by the Paleoproterozoic accretion of several distinct oceanic terranes in connection with the metamorphic basement rocks beneath the Phanerozoic sedimentary cover of the Western Canada Sedimentary Basin (from here on, WCSB) [*Hoffman*, 1988]. The most recent major period of westward expansion began in the Phanerozoic following the commencement of the subduction of the Kula and Farallon Plates, which resulted in the accretion of much of the present-day crust beneath the Canadian Cordillera [*Hoffman*, 1988; *Ross et al*., 1991; *Sears et al*., 2007]. The bulk of the subducted material possibly resides in the lower mantle well east of the present-day continental margin [*Bunge and Grand*, 2000].

Previous research into the structure of the lithosphere and upper mantle beneath the WCSB has benefited from a wide range of geophysical observations. Data from the Canadian National Seismograph Network (CNSN) stations EDM and WALA, which began operating in the early 1990s, provided preliminary constraints on the differential delay times of Moho (*Pms*) and mantle converted phases (P410s, P520s, and P660s) [*Cassidy*, 1995; *Bostock*, 1996; *Eaton and Cassidy*, 1996; *Shragge et al.,* 2002]. Further data were introduced through the Lithoprobe project [*Ross and Eaton*, 2002; *Ross*, 2002], most notably the Slave and Northern Cordillera Lithospheric Evolution transect and temporary deployments such as the Canadian Northwest Experiment [*Mercier et al.,* 2008] and the Batholiths project [*Mercier et al.,* 2009]. The resulting broadband data improved the understanding of craton-Cordillera transition [*Mercier et al.,* 2008; *Dalton et al.,* 2011] and the depth/integrity of lithospheric roots [*Shragge et al.,* 2002]. These deep-probing experiments are complemented by a series of shallow refraction and reflection lines, e.g., the Alberta Basement Transect [*Gorman et al.,* 2002] and the Southern Alberta Refraction Experiment [*Gorman et al.,* 2002; *Clowes et al.,* 2002],

which primarily targeted the basement and crustal structures in the WCSB using active-source techniques [*Gorman et al.,* 2002; *Clowes et al.,* 2002]. A key outcome from these deployments is a significant crustal/mantle seismic gradient from cratons to terranes near the Cordilleran Deformation Front [e.g., *Mercier et al.,* 2008; *Dalton et al.,* 2011], which is generally supported by the shear and compressional speeds from global [*Grand and Helmberger*, 1984; *Grand*, 1994; *Bijward et al.,* 1998; *Grand*, 2002; *Ritsema et al.,* 2004; *Montelli et al.,* 2004; *Obayashi et al.,* 2006; *Simmons et al.,* 2010] and regional [*Grand*, 1994; *Grand et al.,* 1997; *Frederiksen et al.,* 2001; *Shragge et al.,* 2002; *van der Lee and Nolet*, 1997; *Nettles and Dziewonski*, 2008] tomographic inversions. This gradient potentially marks the boundary between the hot mantle beneath the Cordillera, which is often associated with Mesozoic subduction [*Currie and Hyndman*, 2006], and the relatively cold and ancient mantle beneath the North American Craton [*Blum and Shen*, 2004]. The depth of this transition is restricted to the upper mantle in these earlier analyses, though the spatial extent remains debated due to limited resolution of the existing data (especially below 200 km) beneath southern WCSB.

A particularly underconstrained depth range beneath the WCSB is the upper mantle transition zone (for short, MTZ) due to reduced fundamental surface wave sensitivities with depth. This is unfortunate since the details of thermal and chemical anomalies within and above the MTZ are critical for the understanding of the dynamics as well as the tectonic history of western Laurentia. So far, mantle anomalies have been reported in southern WCSB in possible connection with (1) the lingering effects of the Farallon slab on the surrounding mantle [*Schmid et al.,* 2002] or (2) the descending Juan de Fuca Plate at the Cascadia subduction zone [*van der Lee and Nolet*, 1997; *Frederiksen et al.,* 2001]. These proposed mantle anomalies could significantly impact the depths of mineral phase changes from olivine to higher-pressure polymorphs such as wadsleyite (for short, the 410) and ringwoodite (for short, the 520), as well as the condition for the dissociation of ringwoodite to Mg-perovskite and magnesiowustite (for short, the 660) [*Bina*, 2003; *Katsura and Ito*, 1989; *Ita and Stixrude*, 1992; *Helffrich*, 2000; *Katsura et al.,* 2004]. The robustness and characteristics of these proposed structures remain debatable, however, mainly due to the limited number of broadband seismic receivers in the WCSB.

A key metric in the assessment of mantle structure is the depths of MTZ discontinuities, which have long been recognized as sensitive measures of both temperature and composition [e.g., *Shearer and Masters*, 1992; *Deuss*, 2009]. Among the various seismic phases, long-period reflected (e.g., *SS*/*PP* precursors; [*Shearer*, 1991], see *Deuss* [2009] for review) and short-period converted (*S*-to-*P* or *P*-to-*S*) [*Vinnik*, 1977; *Langston*, 1979; *Rondenay*, 2009] waves have been most commonly adopted. In continental regions, the latter phase group is often the method of choice due to its high frequency nature. For instance, using receiver functions [*Rondenay*, 2009] computed from *P*-to-*S* conversions, a recent study by *Thompson et al.* [2011] proposed a relatively flat MTZ beneath the Archean and Proterozoic domains in eastern Canada.

This study presents new constraints on the MTZ and upper mantle structure beneath the Canadian Rockies and Alberta Network (CRANE) of seismic stations near the margin of the North American Craton (Figure 1). By analyzing radial component receiver functions [*Langston*, 1979; *Ammon*, 1991; *Cassidy*, 1992; *Ligorria and Ammon*, 1999], we are able to accurately determine the depths of the MTZ discontinuities and thereby estimate the changes in temperature and composition from craton to terranes/Cordillera in western Canada. Singular Spectrum Analysis (SSA) [*Cadzow*, 1988; *Trickett*, 2003; *Oropeza and Sacchi*, 2011] was applied to individual station gathers for noise attenuation and the interpolation of irregularly spaced data, and least squares parabolic Radon transform (PRT) [*Sacchi and Ulrych*, 1995; *Schultz and Gu*, 2013] was introduced for more reliable detection and assessment of *P*-to-*S* conversions from MTZ discontinuities (e.g., P410s and P660s). The combination of these algorithms and the availability of the regional array provided the basis for an updated model of mantle interfaces beneath southwestern WCSB.

2. Data and Methods

We utilize 18 broadband, three-component seismic stations from CRANE to improve the regional earthquake coverage in western Canada. This semipermanent network [*Gu et al*., 2011] was designed to complement the existing stations at Leduc (EDM, Alberta), Waterton Lake (WALA, Alberta), and Sale Mountain (SLEB, British Columbia), three permanent broadband stations from the Canadian National Seismograph Network (CNSN). With average spacing of ~150 km between stations, these two arrays provide semiuniform coverage beneath the southern WCSB. The main imaging approach used in this study is the receiver

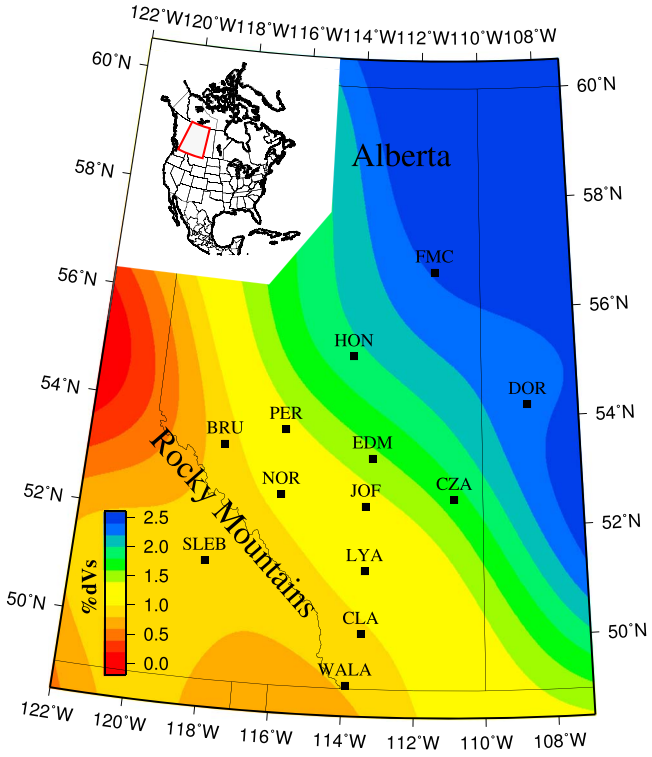

Figure 1. Seismic stations from CRANE and CNSN stations EDM, WALA and SLEB. The background colored map shows the shear velocity perturbations from ND2008 [*Nettles and Dziewonski*, 2008] at 50 km depth.

function technique [*Langston*, 1977; *Vinnik*, 1977; *Ammon*, 1991; *Ligorria and Ammon*, 1999; *Cassidy*, 1995; *Bostock*, 1996; *Liu et al.*, 2003; *Tauzin et al.*, 2008; *Gu et al.*, 2011; *Thompson et al.*, 2011], with critical improvements to counteract the high noise levels caused by soft glacial sediments. The short-period nature of receiver functions computed from *P*-to-*S* converted waves enables high-resolution constraints on the depth and impedance (the product of density and velocity) contrast of crustal and mantle interfaces beneath the seismic stations (see *Rondenay* [2009] for review).

A number of signal processing steps are taken to ensure the accuracy of the depth/thickness measurements (Figure 2). After preprocessing, which included distance sorting, rotation, and deconvolution of three-component seismograms, we obtain radial component receiver functions and introduce time corrections to minimize the effect of the lateral variations in crustal thickness and path velocity. The resulting traces are then partially stacked to improve the signal-to-noise ratio (SNR) such that SSA and PRT could be applied to enhance the mantle conversions. Finally, we perform a depth migration based on a reference Earth model and extract the depths of mantle interfaces from stacked (and depth-migrated) receiver functions (see Figure 2). Most of the procedures outlined above, especially SSA and PRT, are necessitated by the limited data volume and quality in central Alberta. Their details are presented in the following sections.

2.1. Preprocessing

Our data set incorporates over 8800 earthquakes with moment magnitudes greater than 5.5. All events occurred in the time window of 1992–2011 (with 2006 being the start of CRANE array) at source-station

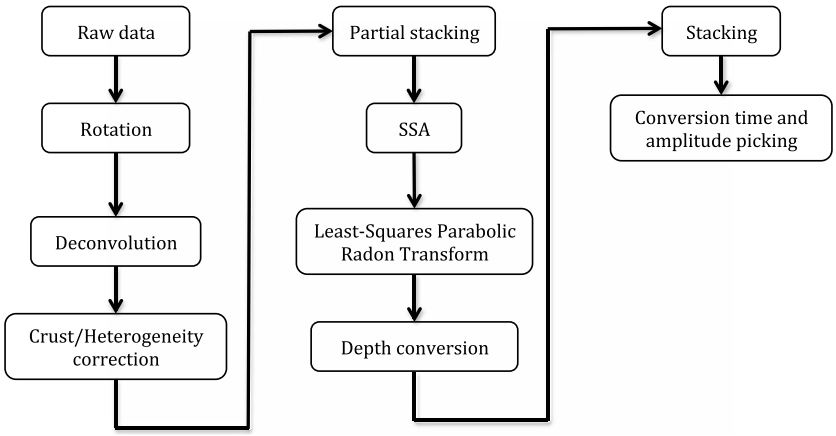

Figure 2. Workflow of the various processing steps to obtain the depths of mantle seismic discontinuities.

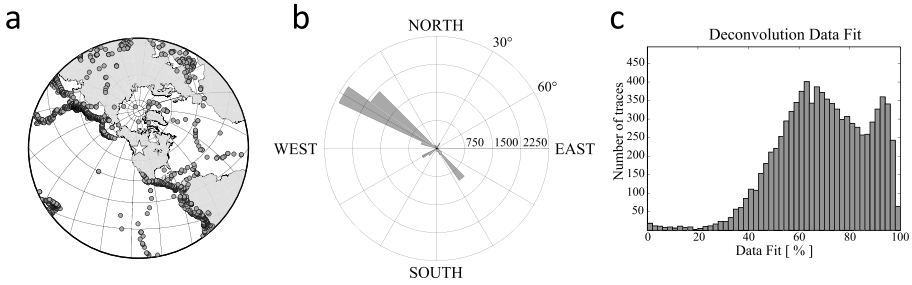

Figure 3. (a) Epicenter locations (grey circles) for all events used in this study. The location of the CRANE array is marked with a star symbol at the center. (b) Back azimuth distribution of our receiver function data set illustrated using the linear scale. The numbers indicate the data count. (c) Percentage data fit for the receiver function data set after time domain iterative deconvolution. The majority of the data fit exceeds 50%.

distances between 30° and 90° (Figure 3a), an ideal range for receiver function analyses [*Langston*, 1977; *Vinnik*, 1977; *Rondenay*, 2009] due to the near-vertical incidence angle of the *P* wave raypaths. After rotating the original components to vertical, radial, and transverse, the resulting seismograms are integrated to displacement and band pass filtered with corner frequencies of 0.07 Hz and 1 Hz. This frequency range was empirically chosen to maximize the energy in the expected arrival window of the P410s and P660s, the main focus of this study. We then compute the signal strength as the standard deviation of the vertical component amplitude in the time window of 1–25 s after the predicted *P* wave arrival time from Preliminary Reference Earth Model (PREM) [*Dziewonski and Anderson*, 1981]. The ratio between this value and that of the noise window, which is similarly defined for the time window of 105–5 s prior to *P*, provides an effective SNR criterion; recordings with SNR less than 2 are subsequently removed. This procedure retains 4846 high-quality event-station pairs, approximately 55% of the original data, for the subsequent analysis of receiver functions. The resulting distribution of back azimuths (Figure 3b) reveals dense coverage in narrow azimuthal ranges of 285°–320° and 135°–160°. Unfortunately, this limited range precludes a comprehensive analysis of the azimuthal variations of MTZ discontinuities.

2.2. Receiver Function Estimation

We apply the iterative deconvolution technique of *Ligorria and Ammon* [1999] to the selected radial and vertical component data traces. The vertical component seismogram is deconvolved from the radial component to minimize source effects and isolate converted *S* wave arrivals. We adopt a Gaussian filter width of 0.8 [e.g., *Crotwell and Owens*, 2005] to maximize the coherence and visibility of P410s and P660s. Up to 500 iterations are performed during the time domain deconvolution to ensure the convergence of the solutions. We permit both positive and negative phases to be added to the deconvolved receiver function and use the data misfit and percentage match (Figure 3c) to the original data to window the data set; receiver functions with data fit percentages below 80% are automatically rejected. This windowing procedure tends to accentuate the quality of the converted phases rather than other dominant interfering phases. In total, 1780 high-quality receiver functions are retained for the final analysis.

2.3. Crust and Mantle Heterogeneity Corrections

To minimize the effects associated with crustal thickness and composition, we compute travel time corrections using CRUST2.0 [*Bassin et al.*, 2000]. This choice of a global model is necessitated by the limited published constraints on crustal depth from regional data. For each event-station pair, travel times are computed by integrating the unperturbed geometrical raypath between the piercing points of *P* and *Pds* at the model Moho depth beneath the station for both PREM and a similar model with a different Moho depth; the resulting travel time difference between these two values is subsequently applied to the corresponding receiver function as a time shift. The effect of upper mantle heterogeneity above the 410 is also minimized by tracing rays through layered shear velocities from ND2008 [*Nettles and Dziewonski*, 2008] and scaled *P* velocities computed from the same model using the *P*/*S* velocity ratio of PREM [*Dziewonski and Anderson*, 1981]. Figure 4 shows the crustal and heterogeneity corrections for all stations. The thickest crust, hence the largest negative correction, resides beneath the foreland belt of the Northern Rockies. The average crustal thickness difference between the foothills of the Rockies (BRU, NOR, SLEB, and

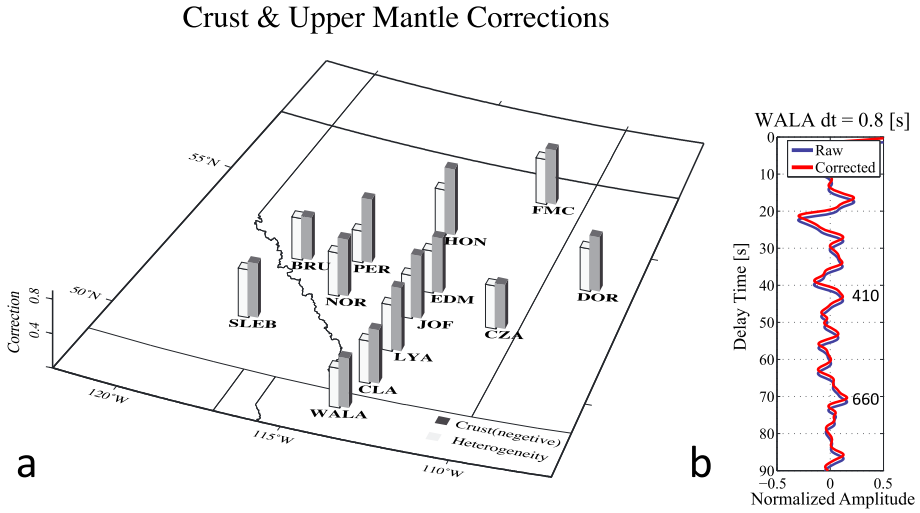

Figure 4. (a) Crust and mantle heterogeneity corrections to the receiver functions. The crustal corrections based on CRUST2.0 [*Bassin et al.*, 2000] are consistently negative while the heterogeneity correction using the ND2008 shear velocity model [*Nettles and Dziewonski*, 2008] is exclusively positive. (b) The approximate amount of time shift and its effect on the receiver functions at a sample station (WALA).

WALA) and the Alberta Basin is ~10 km. To quantify the effect of varying crustal thickness on the observed depth of the MTZ discontinuities, we perform a hypothesis test by "stretching" CRUST2.0 to increase the total thickness by 10 km and recompute the correction for a reference distance of 60°. The resulting crustal correction changes from the reported value (see Table 1) by an average of 0.16 s for every 10 km perturbation in Moho depth, which translates to a modest shift of ~2 km in the depth of the 410. This crustal effect is counteracted by the positive influences from the cold cratonic lithosphere in ND2008 [*Nettles and Dziewonski*, 2008], although the overall correction (see Figure 4) is generally negative due to the magnitude difference between these two corrections. A net negative correction reduces the time difference between the *P* and converted waves, thereby placing the associated mantle interface at a shallower depth.

2.4. Partial Stacking and SSA

In theory, signals from a single receiver function are capable of constraining the depths of crust and mantle interfaces. In practice, however, measurements based on conversions are often unreliable due to the

Table 1. CRANE MTZ Measurements[a]

Station	Latitude (°)	Longitude (°)	410 (km)	± (km)	520 (km)	± (km)	660 (km)	± (km)	410 Amplitude	520 Amplitude	660 Amplitude	Correction (s)	Number
Overall	-	-	419	0.01	534	12	667	0.01	0.0653	0.0224	0.0780	−0.173	1780
FMC	56.7	−111.5	-	-	502	1	662	5	-	0.0162	0.0098	−0.008	29
DOR	54.2	−108.6	415	11	520	0.01	-	-	0.0397	0.0426	-	−0.127	12
HON	55.1	−114.1	419	4	530	8	665	2	0.0465	0.0540	0.0493	−0.016	27
CZA	52.5	−110.9	416	1	523	2	665	2	0.0342	0.0224	0.0199	−0.135	100
EDM	53.2	−113.4	414	0.01	526	1	658	1	0.0595	0.0206	0.0595	−0.147	434
JOF	52.3	−113.5	413	15	520	3	659	5	0.0899	0.0351	0.0589	−0.106	15
PER	53.7	−116.0	422	1	-	-	671	1	0.0392	-	0.0298	−0.239	139
BRU	53.3	−117.9	417	1	533	18	663	15	0.0331	0.0243	0.0209	−0.226	46
NOR	52.5	−116.1	421	2	515	1	664	6	0.0280	0.0195	0.0202	−0.195	114
LYA	51.2	−113.5	411	1	-	-	656	8	0.0373	-	0.0502	−0.157	47
SLEB	51.2	−118.1	420	1	534	7	672	2	0.0447	0.0234	0.0501	−0.367	297
CLA	50.0	−113.5	427	19	516	5	674	2	0.0183	0.0385	0.0598	−0.071	41
WALA	49.1	−113.9	426	0.01	535	14	675	0.01	0.0628	0.0425	0.0918	−0.114	479

[a]Recording station locations and the MTZ discontinuities. Measurements for stations with fewer data (<100) were directly made from summary traces instead of SSA+Radon reconstruction. Empty cells indicate that reliable measurements could not be made.

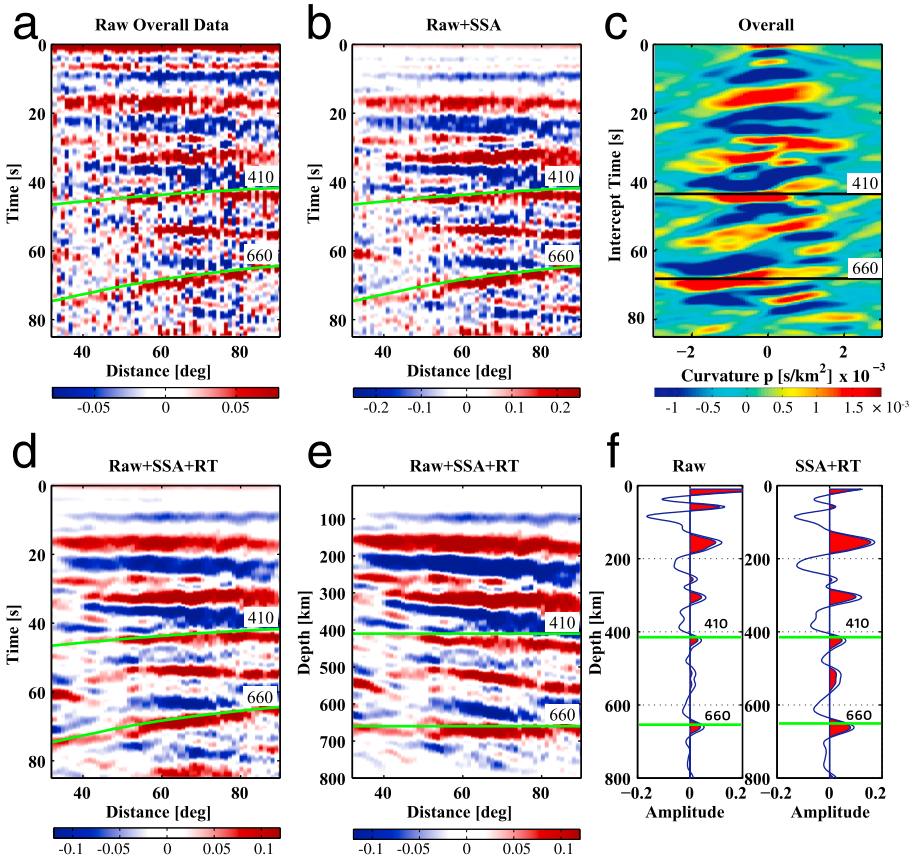

Figure 5. (a) Partially stacked seismograms with noise. (b) Reconstructed data after applying the SSA method. (c) PRT of the SSA reconstructed time series, highlighting a series of prominent mantle conversions. (d) Data reconstructed from the Radon panel. (e) Depth domain migrated data using PREM [*Dziewonski and Anderson*, 1981]. (f) Stacked data in the depth domain for raw and reconstructed receiver functions. The green lines in Figures 5a, 5b, and 5d–5f, as well as dark lines in Figure 5c, indicate the expected arrivals of converted phases P410s and P660s based on PREM.

presence of random noise, scattering, and/or interfering phases. Signal enhancement is vital in this study due to the low overall SNR at temporary seismic stations, which mainly resulted from the thick Phanerozoic cover in southern WCSB. Several steps were taken to enhance the SNR, beginning with a "partial stacking" procedure that performs a running average of receiver functions at each station, regardless of the source-station azimuths, based on epicentral distance. The default averaging window size (or bin width) is 1°, which is heuristically determined to balance the needs of data resolution and noise reduction. The bin centers are spaced 1° apart and do not overlap with one another. Despite significant variations in data volume, this value ensures that each station contains less than 36% empty averaging bins. Figure 5a shows the partial stack of the entire data set where the amplitudes of the signals of interest (e.g., P410s and P660s) are improved by a factor of 3 in the regional gather.

We apply the SSA algorithm to simultaneously remove gaps in the gathers and reduce noise in the individual data traces. SSA, also known as Cadzow filtering [*Cadzow*, 1988; *Sacchi and Ulrych*, 1995; *Trickett*, 2003; *Oropeza and Sacchi*, 2011], is a principle component analysis in the time domain that extracts information from noisy time series [*Schoellhamer*, 2001]. The method comprises of two complementary stages: data decomposition and reconstruction [*Oropeza and Sacchi*, 2011]. The decomposition stage first embeds the original time series into a trajectory matrix and then performs a Singular Value Decomposition [*Golub and Van Loan*, 1989; *Press et al.*, 1992] to determine key properties of the signals such as trends and notable structures. During the second stage, minor singular values of the projection matrix are eliminated (i.e., rank reduction [*Trickett*, 2003]) and reinterpolated; noise-reduced time series are subsequently produced through reconstruction [*Oropeza and Sacchi*, 2011].

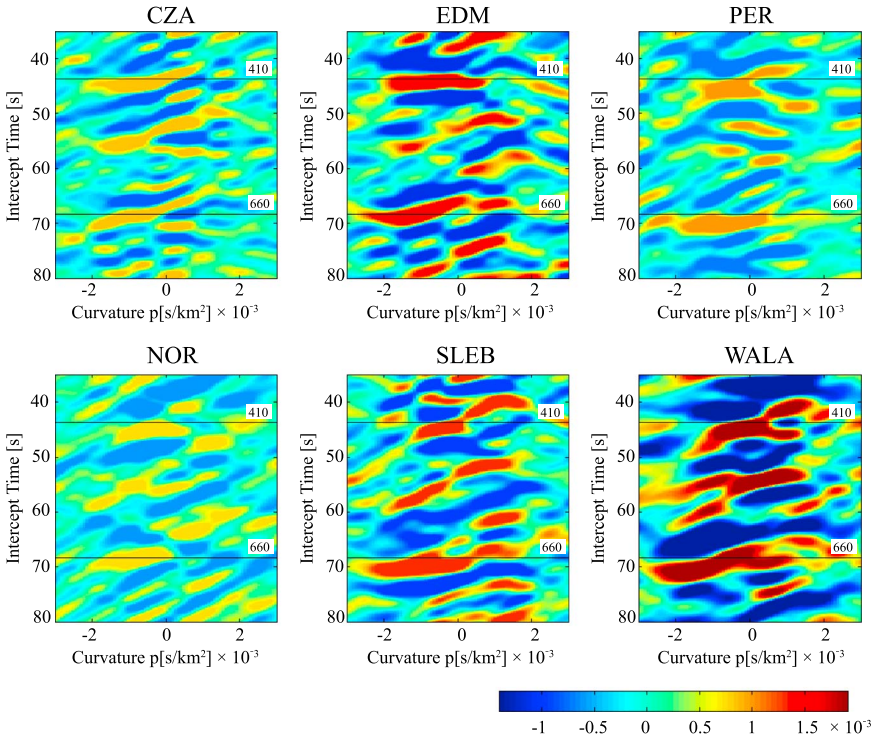

Figure 6. Radon panels computed from six stations with more than 100 receiver functions. The predicted arrival times of the P410s and P660s phases based on PREM are highlighted by horizontal lines.

SSA is a powerful technique applicable to many practical problems involving dynamical systems [*Broomhead and King*, 1986; *Ghil and Vautard*, 1991] and multivariate statistics [*Takens*, 1981]. Since this method is equally effective to individual time series [*Trickett*, 2003] and multidimensional/multivariate data [*Oropeza and Sacchi*, 2011], it is easily adaptable to the time-distance (a proxy for arrival angle) receiver function observations at each seismic station. Our data directly benefit from noise reduction property of SSA through a rank reduction of the projection matrix from the time series. The built-in spatial interpolation during data reconstruction also enhances the robustness and linearity of the converted phases across arrival angles (Figure 5b). In comparison with the original time series, the time series after SSA processing (see Figure 5b) leads to greater stability and accuracy of Radon imaging detailed below.

2.5. Least Squares PRT, Depth Conversion, and Stacking

Time-space domain data gathers after partial stacking, noise reduction, and interpolation are subjected to least squares PRT for reliable, simultaneous constraints on the ray parameters and arrival times of converted phases. PRT is an integral transform that, similar to *H-k* analysis, slowness slant stacking, and vespagram summation [*Zhu and Kanamori*, 2000; *Rost and Thomas*, 2009; *An et al.,* 2007; *Gu and Sacchi*, 2009], projects data in time and offset (t, x) domain onto the Radon (reduced time τ and ray parameter p) domain. When posed as a least squares inverse problem involving individual frequency components and proper regularization [*Schultz and Gu*, 2013], PRT can be a reliable high-resolution tool for signal detection and isolation. We apply PRT to the SSA reconstructed data [*Beylkin*, 1987; *Sacchi and Ulrych*, 1995; *Sacchi*, 1997; *An et al.,* 2007] assuming (1) a reference distance of 60° and (2) an empirically determined regularization parameter μ based on the variable noise level at each station (Figure 5c). For reliable solutions, stations with higher average noise levels (or lower overall signal quality) are damped more severely.

Finally, the reconstructed data traces after crustal corrections (Figure 5d) are converted to depth using PREM [*Dziewonski and Anderson*, 1981] (Figure 5e). This procedure flattens the moveout curves and provides direct inferences on the depths of the MTZ discontinuities. It is worth noting that a change of 1-D reference model from PREM to IASPEI91 [*Kennett and Engdahl*, 1991] only changes the discontinuity depths by 3 km and 4 km, respectively, for the 410 and 660 (see Figure S1 in the supporting information). The modeled data from PRT

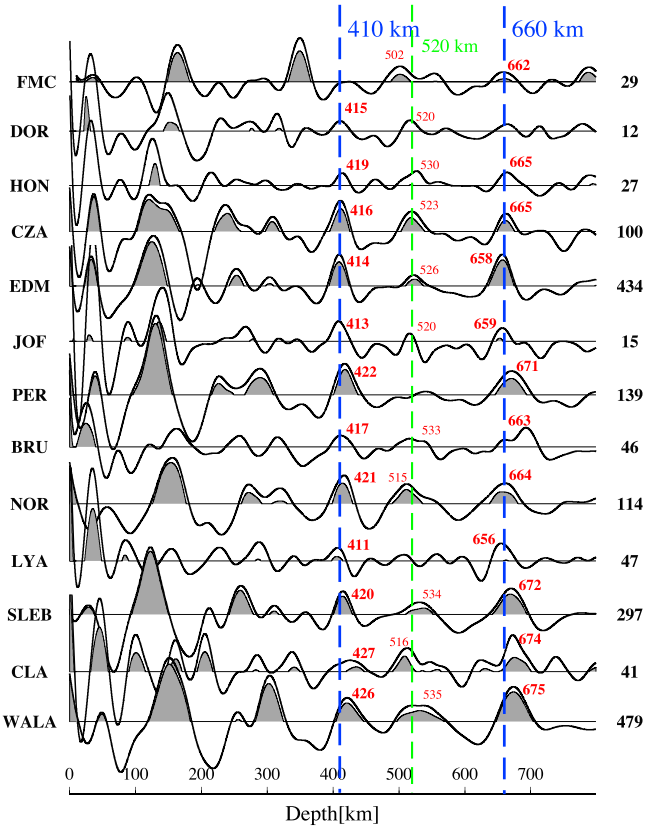

Figure 7. Stacked, depth-converted receiver functions from stations analyzed in the study. The numbers on the right of the traces indicate the number of receiver functions in the stack. The black line is the summary trace, and the shaded areas indicate the energy of stacked data minus one standard deviation. The blue dashed lines indicate the depths of 410 km, 520 km, and 660 km.

(see Figures 5c and 5d) forward operation preserve the major phase characteristics of the time-distance profile. The nonlinear moveout curves for the P410s and P660s arrivals are clearly recognizable in the input and modeled data gathers. Further enhancements to data quality through SSA and PRT are evident from (1) more consistent phase moveout in the migrated stacks relative to the raw time domain signals (see Figures 5a and 5e) and (2) more robust conversions from mantle interfaces (Figures 5f and 6). We estimate the uncertainties of the MTZ converted waves using a bootstrapping approach [e.g., *Gu and Dziewonski*, 2002; *Gu et al.,* 2003] based on the distribution of automatic depth measurements from 200 trials. In each trial, a depth measurement (e.g., of P660s) is made based on the stack of the same number of depth-migrated receiver functions randomly drawn from the actual data set; it should be noted that a single receiver function is allowed to be selected multiple times. The uncertainties of P410s and P660s, which are estimated using one standard deviation of the respective bootstrapping distributions, decrease significantly as the result of the SSA and PRT operations (Figure 7). The improvement in the clarity of the converted phases based on partial stacking, SSA, and PRT is more significant for stations with above-average data volume. The three permanent stations (EDM, WALA, and SLEB) show moderately higher SNR than the regional average, while 6 out of 13 stations with more than 100 traces show mantle conversion amplitudes well above the background noise levels (see Figure 7).

3. Result

The arrival times, discontinuity depths, and the associated uncertainties for all stations are reported in Table 1. The depth uncertainties of the station measurements are generally 3 km or less, though larger numbers are obtained for stations with limited numbers of high-quality recordings (e.g., JOF and DOR) or a complex underlying mantle structure (e.g., WALA and BRU). The regional averages based on the same procedure and the aggregate of all receiver functions are particularly well constrained, showing bootstrapping uncertainties of 0.01 km or less due to more effective data averaging than individual stations (see Table 1).

From the regional solution we obtain average MTZ discontinuity depths of 419.0 km and 667.0 km for the 410 and 660, both are deeper than the respective global averages of 409–410 km and 650–660 km [*Gu et al.,* 2003; *Deuss and Woodhouse*, 2002; *Houser et al.,* 2008; *Houser and Williams*, 2010]. The resulting MTZ thickness is 248 km, which is 6 km thicker than the global average [*Flanagan and Shearer*, 1998; *Gu et al.,* 2003; *Lawrence and Shearer*, 2006; *Tauzin et al.,* 2008]. Both the 410 and 660 discontinuities are deep beneath western Alberta (Figures 8a and 8b), showing considerable lateral variations from cratons in the northeast to Cordillera in the west and southwest (Figures 8c and 8d). Energetic arrivals are also present in the

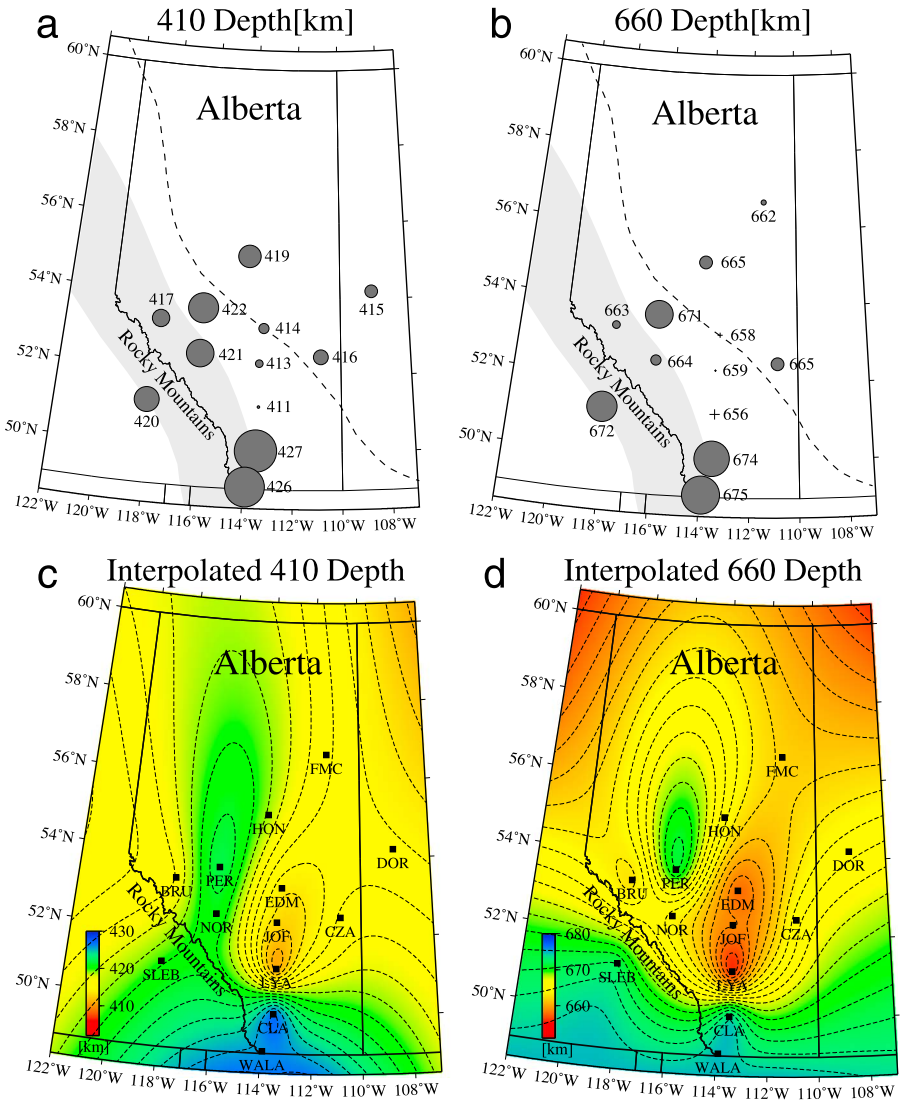

Figure 8. The measured MTZ discontinuity depths. The shaded region denotes the location of the Rocky Mountains. The dashed black line indicates the 1.5% shear velocity perturbation from model ND2008 at 50 km depth, which may be interpreted as the approximated edge of the North American Craton. The filled circles and crosses show the respective positive and negative depth perturbations to the regional averages. (a) The depth of the 410 for each station. (b) The depth of the 660 for each station. (c) The interpolated depth of the 410. (d) The interpolated depth of the 660. The large-scale patterns are generally consistent between the two discontinuities.

middle of the transition zone, ranging from 502 to 535 km, in all but two stacked receiver functions (see Figure 7 and Table 1). Mid MTZ discontinuities are known to be weak [*Gu et al.*, 1998] or complex [*Deuss and Woodhouse*, 2002] under major continents. The majority of the arrivals (e.g., from stations CZA, CLA, JOF, and NOR) show simple P520s pulse shapes, and the average depth and amplitude of P520s are 534 km and 2.24%, respectively.

An effective measure to mitigate uncertainty and ambiguity during the interpretation of MTZ converted wave arrivals is the differential times of P660s and P410s, which approximates the MTZ thickness (Figure 9), due largely to the overlapping P410s and P660s ray segments beneath a given station. Figures 9a and 9b show the computed MTZ thickness values across the array before and after, respectively, correcting for MTZ heterogeneity using ND2008. A distinct north-south zonation is visible relative to an average MTZ thickness of 246.2 km. The width of the MTZ beneath northern-central Alberta is comparable to global averages from *SS* precursors (242 km [*Flanagan and Shearer*, 1998; *Gu and Dziewonski*, 2002; *Lawrence and Shearer*, 2008])

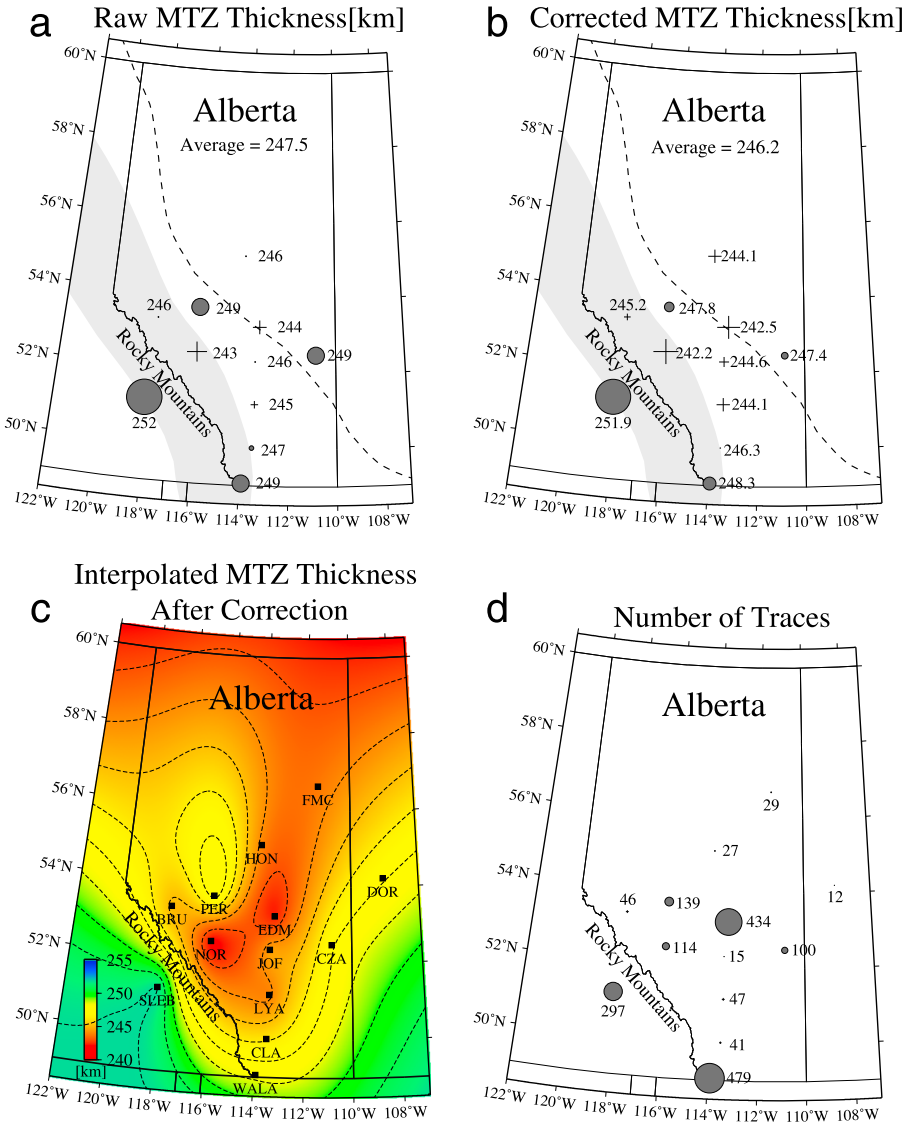

Figure 9. MTZ thickness estimates based on receiver functions. The shaded region highlights the Canadian Rockies. The dashed black line delineates the +1.5% shear velocity contour from model ND2008 at 50 km, marking the approximated edge of the craton(s). The filled circles show values greater than average, and the crosses mark locations where our results are below average. (a) The MTZ thickness obtained by subtracting the discontinuity depths. (b) The MTZ thickness after the MTZ heterogeneity correction. (c) The corrected MTZ thickness after spatial interpolation. (d) The number of receiver functions in the corresponding stack.

and *P*-to-*S* conversions [*Lawrence and Shearer*, 2006; *Tauzin et al.*, 2008], though the most reliable stations with the largest number of traces (e.g., EDM: ~242.5 km, WALA: ~248.3 km, and SLEB: ~251.9 km) indicate gradual thickening from cratons (NE) to Cordillera (SW). This pattern resembles that of the travel time corrections from mid MTZ heterogeneities predicted by ND2008, which are consistently negative (slow) but the magnitude of the correction increases notably to the northeast. The average correction values correspond to a thickness adjustment of 2.6 km or less, which have only minor influences on the key features in MTZ thickness (e.g., an anomalously thick MTZ) beneath the southern stations.

The difference between our values and the results obtained by global studies is highlighted in Figure 10. The depths of the 410 and 660 are compared against their experimentally determined values based on the Clapeyron slopes of olivine to wadsleyite (+3.2 MPa/°K) and ringwoodite to magnesiowustite + perovskite (−2.0 MPa/°K) [*Helffrich*, 2000] phase transformations. Results from earlier studies of *SS* precursors [*Gu et al.*, 2003; *Houser et al.*, 2008] are clustered below the theoretical curve, which suggest a shallow 660, while

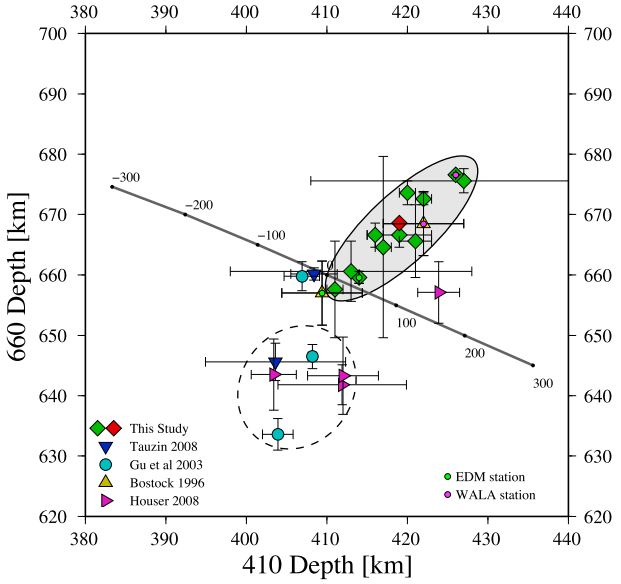

Figure 10. The depths of the 410 and 660 beneath the study region from various studies. The green diamonds indicate the values from this study, and the red diamond marks the position of the regional average. The yellow triangles show the results of *Bostock* [1996] for stations EDM and WALA based on *Pds* receiver functions. These two stations are highlighted using small green and pink circles, respectively. The blue inverted triangles show the results of stations FFC (Fort Churchill, MB) and LLLB (Lilloet, BC) from *Tauzin et al.* [2008] using a similar approach. The discontinuity depths from *Gu et al.* [2003] and *Houser et al.* [2008] based on *SS* precursors are indicated using cyan circles and magenta arrows, respectively. The contrast between earlier estimates from low-resolution global studies and those of this study is highlighted by the unfilled and shaded ellipses, respectively. The thick grey line represents the expected values for the 410 and 660 while assuming (1) the Clapeyron slopes from *Helffrich* [2000] and (2) a continuous thermal anomaly that affects both phase boundaries.

measurements from receiver functions [*Bostock*, 1996; *Tauzin et al.,* 2008] mainly reside above the predictions at comparable pressures. Our regional measurements are highly consistent with those from earlier studies of receiver functions, particularly *Bostock* [1996]. The notable depth difference between studies of long- and short-period waves likely results from the distinct imaging scales where local-scale variations of receiver functions may have been largely averaged out by the long-period *SS* precursors.

4. Discussion

4.1. General Assessment

Recent studies of the structure of the MTZ beneath the northeastern Canadian portion of the North American Craton have revealed a simple MTZ relatively devoid of major thermal or compositional variations in the upper mantle [*Bostock*, 1996; *Thompson et al.,* 2011]. By analyzing receiver functions from a dense regional array around the Hudson Bay, *Thompson et al.* [2011] demonstrated that both MTZ discontinuities are elevated beneath the craton and depressed slightly toward the margins. The thickness of the MTZ remains roughly constant, which is interpreted as evidence of a flat MTZ [*Thompson et al.,* 2011] beneath the cratonic interior well northeast of our study region. In comparison, mantle layering west of our study region is considerably more complex, as evidence from long-period analyses of global *SS* precursors [*Flanagan and Shearer*, 1998; *Gu et al.,* 1998, 2003], *PP* precursors [*Chambers et al.,* 2005; *Deuss*, 2009], and intermediate-period receiver functions [*Lawrence and Shearer*, 2006] generally indicates reduced MTZ thicknesses in response to a hot upper mantle beneath the Pacific Ocean basin. The interplay between the broadly averaged low-velocity zone and more localized thermal structures, e.g., a thin low-velocity layer above the 410 and high velocities [*Schaeffer and Bostock*, 2010] within the descending Juan de Fuca Plate, highlights the complex seismic structure and layering west of the Cordillera. In comparison, constraints on the mantle layering beneath the WCSB and Cordillera remain a work in progress. While global discontinuity maps [e.g., *Flanagan and Shearer*, 1998; *Gu et al.,* 2003; *Lawrence and Shearer*, 2008] suggest a relatively flat MTZ, diminished discontinuity topography could be partially attributable to the averaging effects of large Fresnel zones [*Neele et al.,* 1997]. The use of higher-resolution approaches such as receiver functions was previously limited to sparsely populated national network stations [*Cassidy*, 1995; *Bostock*, 1996], linear temporary arrays [*Shragge et al.,* 2002; *Courtier et al.,* 2006], or crustal-scale investigations [*Clowes et al.,* 2002; *Bostock et al.,* 2010; *Cassidy*, 1995].

The stations used in this array significantly improve the regional data coverage, from which the receiver function data shed new light on the craton-Cordillera transition in southwestern Canada. In contrast to eastern Canada, the mantle structure and stratification above the MTZ are strongly variable in a relatively confined region between the Alberta Basin and the Rocky Mountain foreland belt. Both the 410 and 660 are depressed and exceed the level of perturbations reported in previous global estimates for the same region. The apparent topographic correlation between these two boundaries cannot be fully

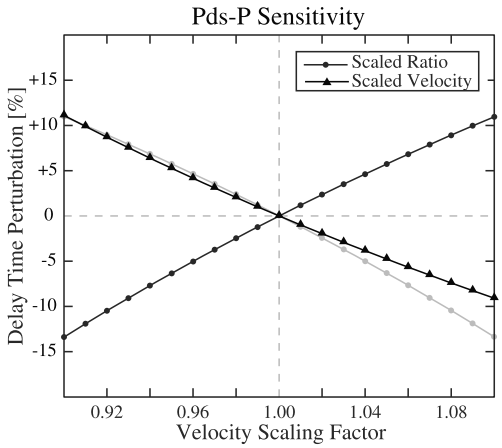

Figure 11. Sensitivity of receiver function delay time perturbations to upper mantle thermal anomalies. The filled circles show the result of scaling both V_P and V_S while maintaining a constant V_P/V_S ratio. The triangles denote the outcome of scaling the V_P/V_S ratio, and the grey line shows a mirrored image of the result (i.e., flipped) while assuming a constant ratio.

accommodated by a vertically continuous thermal anomaly through the MTZ [*Gu and Sacchi*, 2009; *Deuss*, 2009], i.e., upper mantle heterogeneities that strongly influence the common *S* ray segment of P410s and P660s beneath stations likely persist after the tomography-based travel time corrections. Two related factors may be responsible for this observation: (1) the difficulty of accurately ascertain amplitude information using ray theoretical kernels [*Li and Romanowicz*, 1996; *Zhou et al.,* 2004; *Liu and Gu*, 2012], especially in view of a steep gradient in temperature and composition between the remnant of Precambrian cratons and the much younger terranes and Cordillera, and (2) extensive smoothing during tomographic inversions for regions such as Alberta where the data coverage is limited.

4.2. Structure Above the 410

Self-consistent evidence is provided by the regional variation of discontinuity depths for stations residing in the southwest of the study region, particularly those along the Rocky Mountain foreland belt (e.g., PER, BRU, NOR, WALA, SLEB, and CLA). The average depths measured at this cluster of stations are ~422.2 km and 669.8 km, respectively, for the 410 and 660; these are 7.5–9 km greater than the average of the remaining stations. This regional topographic pattern is correlated with the predicted seismic velocity variations in the lithospheric mantle, where the reported contrast between the low-velocity Cordillera and the high-velocity Archean/Paleoproterozoic interior is among the sharpest on the global scale [*Nettles and Dziewonski*, 2008]. This prominent northeast to southwest transition has been an essential fixture in global [*Grand*, 1994; *Grand et al.,* 1997] and regional [*van der Lee and Nolet*, 1997; *Frederiksen et al.,* 2001; *Nettles and Dziewonski*, 2008; *Mercier et al.,* 2009] tomographic inversions, and its signature may persist down to 400 km depth and below [*Mercier et al.,* 2009]. Based on our receiver function analysis, the excess topography of the MTZ discontinuities could imply even greater influences from the model accuracy of Moho depth and upper mantle heterogeneity. Corrections due to crustal thickness variations are generally negative, which has the equivalent effect of elevating the MTZ interfaces (see Figure 4), and may be more significant than the previous estimates (e.g., CRUST2.0 [*Bassin et al.*, 2000]) according to the updated crustal models of *Gu et al.* [2011, 2012] using an improved regional seismic database. Still, the difference in the model corrections is no more than 0.367 s (0.136 s on average), which amounts to 1.25–3.25 km perturbation in discontinuity depth and fails to explain the observed depths of the MTZ discontinuities.

The choice of 1-D reference model in depth migration may also influence the absolute depths, though our synthetic tests based on PREM and IASP91 only show a modest difference of ~3 km (supporting information Figure S1). The effect of the heterogeneity correction for the top 410 km of the mantle is positive, which counteracts the influence of the crustal corrections, due to the above-average velocities in the upper mantle portion of ND2008 in this region. As indicated by Figure 11, increasing both the *P* and *S* velocities reduces the differential time relative to PREM. The sum of the crustal and mantle corrections needs to be more negative to reconcile the discrepancy in delay times and accommodate the overall depression of the MTZ discontinuities. In other words, both upper mantle thermal and compositional variations are likely present, in addition to those predicted by the published tomographic models. The necessary adjustment to the correction for mantle structure above the 410 may be accomplished by (1) a reduction of the absolute velocities while maintaining a constant V_P/V_S ratio or (2) increasing the V_P/V_S ratio used to scaled the shear velocity profile. Either operation or a combination of the two would increase the differential time relative to PREM, especially beneath the Canadian Cordillera, and thereby increasing the nominal discontinuity depth. The combination of velocity reduction and a V_P/V_S ratio increase likely requires diffuse partial melt or increased water content in the mantle above 410 km [*van der Lee and Nolet*, 1997].

To quantify the necessary velocity perturbations for the observed delay times, we compute the vertical incidence delay times using PREM isotropic shear velocities as the background model under both thermal and compositional considerations. We first calculate the theoretical delay time anomaly by increasing both *P* and *S* velocities while keeping their ratio constant and then perform a similar experiment by fixing the shear velocity while varying V_p. The resulting curves show opposite slopes, and the delay time grows proportionally to the V_p/V_s ratio and decreases with an increase in absolute velocity. To assess the relative strength of these two approaches, we construct the V_p/V_s curve in reverse, and the resulting positive delays show comparable amplitudes and trends to those expected from a constant ratio; the effect of the scaled V_p/V_s ratio becomes slightly more pronounced as delay time decreases. This sensitivity test (see Figure 11) suggests three probable causes of the residual MTZ discontinuity topography: (1) a ~2.5% decrease in both V_p and V_s, (2) an increase in the V_p/V_s ratio of ~2%, or (3) a combination of the two. All three candidates are capable of producing a sharper lateral change between cratons and Cordillera, and the required velocities may be accommodated by pockets of partial melt or volatiles in the lithosphere and/or asthenosphere. A hydrated upper mantle, in connection with the nearby Cascadia subduction along the Pacific west coast or the Mesozoic era subduction of the Kula and Farallon Plates, offers a convenient and viable explanation.

The possibility of localized thermal and/or compositional variation in the vicinity of the 410 cannot be excluded, however. The presence of a low-velocity layer atop the 410 [*Bercovici and Karato*, 2003; *Tauzin et al.,* 2010] has the equivalent effect of distributed melt in depressing both discontinuities. A hydrous layer has been reported near the 410 [*Bercovici and Karato*, 2003; *Jasbinsek and Dueker*, 2007; *Tauzin et al.,* 2010; *Schaeffer and Bostock*, 2010; *Schmandt et al.,* 2012] in East Asia [*Huang and Zhao*, 2006], which potentially provides the source of partial melting for the Changbai and Wu Da Lian Chi hot spots [*Zhao*, 2001]. A similar layer has also been suggested to reside within the Tonga slab [*Zheng et al.,* 2007], east of the Nazca-South America subduction zone [*Schmerr and Garnero*, 2007; *Contenti et al.,* 2012], and beneath western Canada [*Schaffer and Bostock*, 2010].

A possible melt layer in connection with southern Alberta is consistent with the hypothesis of *Jasbinsek and Dueker* [2007], a study of receiver function data from a dense array a few hundred kilometers south of our study region. The presence of an intermittent low-velocity, fluid-rich layer was supported by a subsequent study [*Schmandt et al.,* 2011], though the mantle shear velocities beneath northern Cordillera have been highly variable and inconclusive. Some studies favor increased velocities above the 410 [e.g., *Schmandt et al.,* 2012; *van der Lee and Nolet*, 1997], while others proposed average [*Nettles and Dziewonski*, 2008] or below-average velocities [*Simmons et al.,* 2010]. Among the four published models, the velocity map of *Simmons et al.* [2010] appears to be the most consistent with our measured topography on the 410. Part of the disagreement (e.g., a depressed 410 in this study and an uplifted 410 in *Schmandt et al.* [2012]) may be evidence of strong lateral temperature/compositional variations [*Schmandt et al.,* 2012], though undersampling in northern Montana and surrounding regions could be partially responsible due to limited operating time (2 years) of the USArray and relatively few active source experiments in Montana [*Levander et al.,* 2005].

4.3. Reflection Amplitude

While our study mainly focused on the topography of the MTZ discontinuities, there are other informative measures of mantle temperature and composition from regional *P* wave conversions. One such measure is the amplitude of converted waves, which is sensitive to the impedance (i.e., the product of velocity and density) contrast across a mantle interface. In our study region, the ratio between *Pds* and *P* ranges between 0.98% and 8.99% for the two MTZ discontinuities (Figure 12a). With correlation coefficients less than 0.4, the depths of the two MTZ discontinuities and the respective conversion amplitudes are only weakly related statistically (Figures 12b and 12c). Geographically, the amplitude increases substantially toward the southwest, though this seemingly robust observation is confounded by a positive correlation between conversion amplitude and data volume (supporting information Figure S2). The data volume dependency of depth is most severe in the northeastern section (e.g., DOR, FMC, HON, and JOF), where the number of quality receiver functions per station falls below 50. The correlation also depends on the data type: for instance, P660s exhibits a significantly higher correlation with data volume than P410s (see supporting information Figure S2). For these reasons we limit our discussions to well-resolved regions

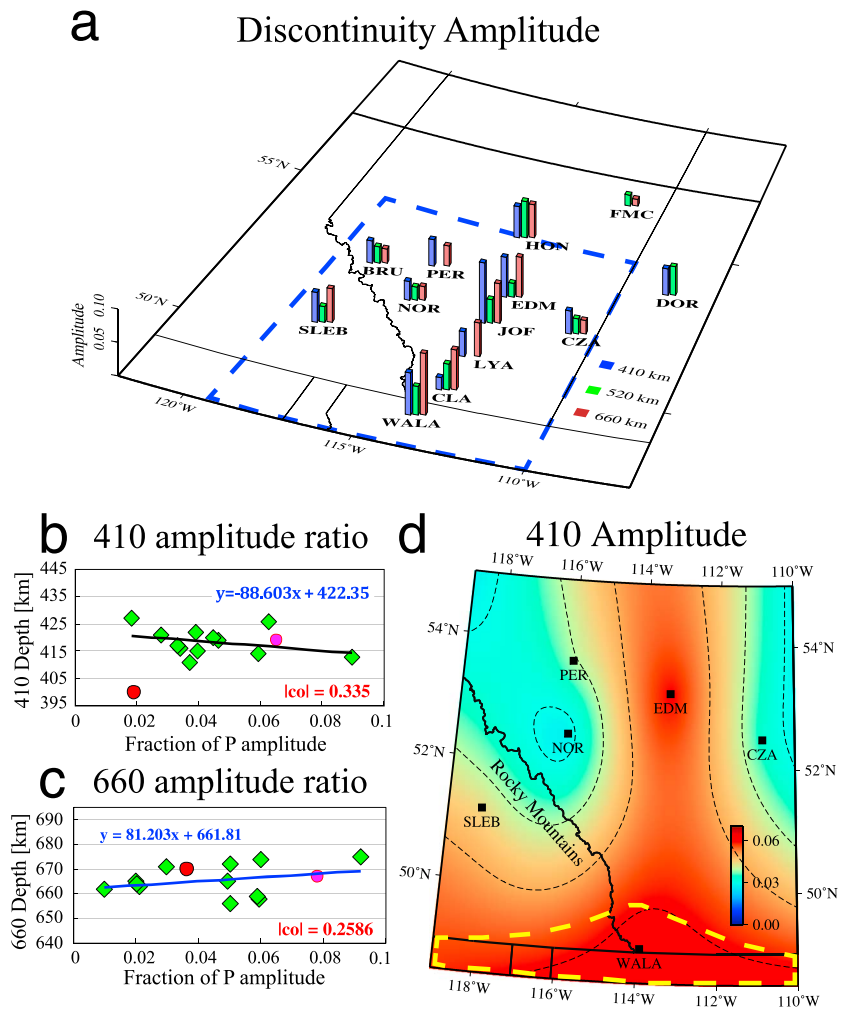

Figure 12. (a) A perspective view of the amplitudes of P410s, P660s, and P520s (see Table 1) after normalization by the regional maximum. (b) A comparison between the amplitude and depth of the 410. (c) A comparison between the amplitude and depth of the 660. The pink circles indicate the global averages, and red circles show the predicted values based on PREM. co = correlation coefficient. The amplitudes and depths do not show a significant correlation with each other. (d) The interpolated amplitude of P410s from six stations with the number of traces in excess of 100. The colorbar values indicate the relative amplitude ratio between P410s and P. The dashed yellow area in the southernmost Alberta, which is the area of the largest regional 410 depression, may contain water or melt at depths below the mantle lithosphere.

surrounding the 410 where data count exceeds 100 (see Figures 12b and 12d). The amplitude variation of the subregion remains complex, as was previously documented on the global scale [e.g., *Flanagan and Shearer*, 1999], though the *S* conversion amplitude relative to *P* in the well-covered southern Alberta (near station WALA) is 4.36% larger than the predicted value of 1.92% from PREM. The excess amplitude indicates increased impedance contrast across the 410 and, in combination with a deep 410 (see Figures 8c and 12d), could strengthen the argument for increased mantle fluids atop the phase boundary (see section 4.2), especially in the southernmost Alberta.

4.4. MTZ Thickness

Unlike the absolute depths of the 410 and 660, which are strongly affected by the structures above the MTZ, the difference between P660s and P410s delay times (or MTZ thickness) is a robust measure of seismic velocities within the MTZ. Earlier studies that included data from this region generally inferred gradual thinning of the MTZ from the Cordillera [*Bostock*, 1996; *Tauzin et al.*, 2008] to an average value beneath the core of the North American Craton. Our results provide further evidence for a relatively mild craton-Cordillera transition and minimal thermal influence from craton(s) [*Thompson et al.*, 2011] at depths below

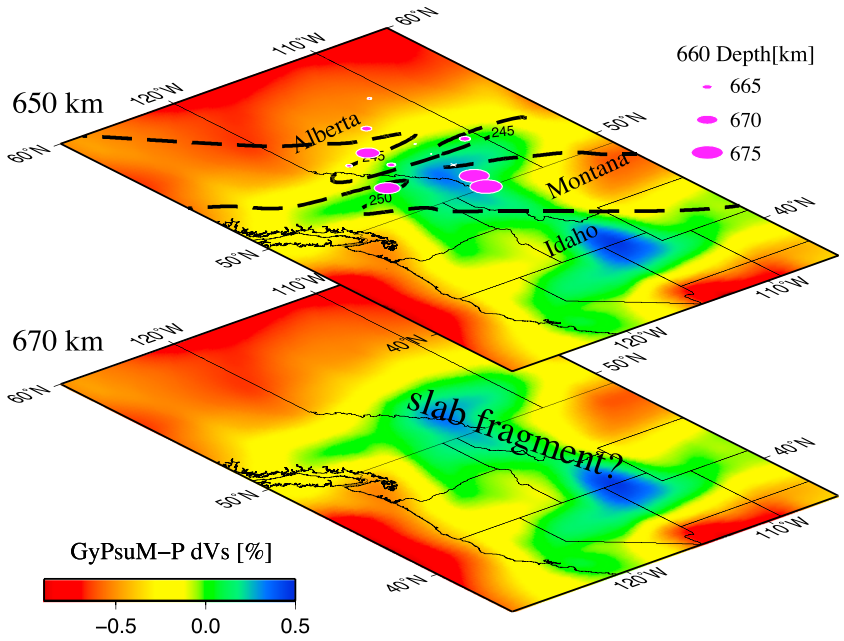

Figure 13. Shear velocities at 650 km, and 670 depth based on GyPSuM [*Simmons et al.,* 2010]. A localized high-velocity anomaly (green and blue colors) is present in southern Alberta, Idaho, and Montana. The depths of the 660 from this study are superimposed on the velocity maps. The dashed contour lines indicate the thickness of the MTZ. The increased MTZ thickness in the southernmost Alberta is caused by a strongly depressed 660, which coincides with the increased shear velocities at the base of the upper mantle in GyPSuM. Both observations could be caused by the presence of a Mesozoic slab fragment.

the asthenosphere (see Figure 9b). The average MTZ thickness (246.2 km) is comparable to the averages of 246 km and 247 km obtained by previous analyses of *Pds* [*Lawrence and Shearer*, 2006; *Tauzin et al.,* 2008] and a value of 242 km obtained using *SS* precursors [*Flanagan and Shearer*, 1998; *Gu and Dziewonski*, 2002]. Systematic MTZ thickness differences resulting from wave types (i.e., *Pds* versus *SS* precursors) have been previously documented by *Lawrence and Shearer* [2006] and *Tauzin et al.* [2008] and are generally attributed to the preferential sampling of continental (rather than oceanic) mantle by the receiver functions.

An interesting feature is in southern Alberta, especially near stations WALA and SLEB, where the MTZ is significantly thicker than regional average. This local thickening resulted from a strongly depressed 660, which suggests the presence of a high-velocity zone at the base of the upper mantle. In view of the Mesozoic tectonic history of North America, this high-velocity signature may be caused by the remnant of the subducted Farallon/Kula Plate. In fact, earlier studies based on different data types [*Bostock*, 1996; *Melbourne and Helmberger*, 2002; *Courtier et al.,* 2006; *Schmandt et al.,* 2012] have revealed fragments of Mesozoic slabs in various parts of the North American continent. Residual thermal anomaly from subduction could account for a local temperature difference of 400°C [*Schmid et al.,* 2002]. This value is closer to thermal equilibrium than an actively subducting slab but remains capable of causing an upward of 19 km depression on the 660 based on experimentally determined Clayperon slope of −2.0 MPa/K [*Helffrich*, 2000]. In other words, an equivalent thermal anomaly from seismic tomography is well within the range exhibited by the average depth perturbation of 13.7 km on the 660 in southern Alberta. The depth of the 660 (Figure 13) is in reasonable correlation with a high-velocity structure from *Simmons et al.* [2010]. The thickened MTZ segment in southern Alberta approximately coincides with a semicircular high-velocity zone in the lower MTZ, which eventually extends into southern-central U.S. (see Figure 13). The presence of a small, abandoned, and unequilibrated slab fragment in the MTZ is a plausible explanation. It also provides a potential MTZ source for dewatering and melting near the top of the 410 in a fashion resembling those of stagnant slabs beneath northeastern Asia [*Zhao*, 2004; *Huang and Zhao*, 2006; *Gu et al.,* 2012], assuming that the thermal anomaly is vertically discontinuous from the base to the top of the MTZ [*Schmandt et al.,* 2012].

Finally, our receiver function stacks show compelling evidence for a single mantle conversion within the MTZ. While the nature of these mid MTZ reflectors is still debated [*van der Meijde et al*., 2003, 2005; *Courtier and Revenaugh*, 2007], results from high-pressure mineral physics experiments have widely suggested olivine phase transitions from wadsleyite to ringwoodite [*Bina and Wood*, 1987; *Rigden et al*., 1991; *Helffrich*, 2000; *Bina*, 2003] and majorite garnet to Ca-perovskite [*Ita and Stixrude*, 1992] as possible mechanisms. The former transition is expected to occur in the depth range of 500–560 km [*Gu et al.,* 1998; *An et al.,* 2007; *Helffrich*, 2000; *Bina*, 2003], which are in excellent agreement with the average of the mid MTZ reflections from this study. The amplitude of this reflection is 0.0224, which is 28.7% of the average amplitude of the 660. Among the best-resolved regions, the most robust conversions from the 520 are observed in southern Alberta Basin, especially at stations CLA and WALA. Increased conversion amplitudes could result from reduced sharpness due to the presence of fluid, as documented by *Courtier et al.* [2006] in eastern U.S., though better station and data coverage than that available to this study will be necessary to verify this result. The simplicity of the 520 is supported by *Schmandt et al.* [2012], though the amplitude and depth of the 520 are considerably larger than those of the earlier study. Our data do not show a clear MTZ conversion below 550 km [*Deuss and Woodhouse*, 2002], which may reflect limited data coverage or increased width of the majorite garnet to perovskite transition [e.g., *Weidner and Wang*, 1998].

5. Conclusion

By analyzing more than 5 years of continuous recordings from CRANE and CNSN stations, we have been able to reliably determine the mantle layering beneath the craton-Cordillera boundary zone in western Canada. The outcomes of this study shed new light on the thermal and compositional variations surrounding the two major MTZ phase boundaries. The key observations and their implications for the mantle structure and dynamics are summarized as follows:

1. Both the 410 and 660 km seismic discontinuities are strongly depressed in the Alberta Basin and eastern Cordillera, showing similar topographic patterns and strong influence from velocity heterogeneities in the mantle above the MTZ. Large depressions and increased impedance contrast on the 410 implies diffuse or localized compositional variations (e.g., partial melt) in the southernmost Alberta.
2. Substantial depressions of the 660 and a locally thick MTZ in the southernmost Alberta indicate decreased temperature at the base of upper mantle. This may be associated with the presence of a relic Mesozoic slab(s).
3. A single *P*-to-*S* conversion is observed near 520 km depth beneath southern WCSB.

In summary, the absolute and differential depths of the two major MTZ phase boundaries are strong functions of mantle temperature beneath the western boundary of the North American Craton. While the data coverage remains a work in progress in southern WCSB, the existing seismic database from an improved regional network can, and will continue to, provide critical inferences about the temperature and composition within and below the mantle lithosphere.

Acknowledgments

We thank Luyi Shen and Ryan Schultz for their assistance with data handling and field deployments for the CRANE array. We also thank two anonymous reviewers and the Associate Editor for their insightful suggestions and comments. The seismic data are publicly available from IRIS data manage center. Many of the figures were generated using the Generic Mapping Tools (GMT) [*Wessel and Smith*, 1998]. This research is supported by the Helmholtz-Alberta Initiative, China Scholarship Council (CSC), and the Canadian National Science and Engineering Council (NSERC).

References

Ammon, C. J. (1991), The isolation of receiver effects from teleseismic *P* waveforms, *Bull. Seismol. Soc. Am.*, *81*(6), 2504–2510.

An, Y., Y. J. Gu, and M. D. Sacchi (2007), Imaging mantle discontinuities using least squares radon transform, *J. Geophys. Res.*, *112*, B10303, doi:10.1029/2007JB005009.

Bassin, C., G. Laske, and G. Masters (2000), The current limits of resolution for surface wave tomography in North America, *Eos Trans. AGU*, *81*, Fall Meet. Suppl. F897.

Bercovici, D., and S. I. Karato (2003), Whole-mantle convection and the transition zone water filter, *Nature*, *425*, 39–44, doi:10.1038/nature01918.

Beylkin, G. (1987), Discrete Radon transform, *IEEE Trans. Acoust. Speech Signal Process.*, *ASSP-35*, 162–172.

Bijward, H., W. Spakman, and E. R. Engdahl (1998), Closing the gap between regional and global travel time tomography, *J. Geophys. Res.*, *103*(B12), 30,055–30,078, doi:10.1029/98JB02467.

Bina, C. R. (2003), Seismological constraints upon mantle composition, *Treatise Geochem.*, *2*, 39–59.

Bina, C. R., and B. J. Wood (1987), Olivine-spinel transitions: Experimental and thermodynamic constraints and implications for the nature of the 400-km seismic discontinuity, *J. Geophys. Res.*, *92*(B6), 4853–4866.

Blum, J., and Y. Shen (2004), Thermal, hydrous, and mechanical states of the mantle transition zone beneath southern Africa, *Earth and Planet. Sci. Lett.*, *217*(34), 367–378, doi:10.1016/S0012-821X(03)00628-9.

Bostock, M. G. (1996), A seismic image of the upper mantle beneath the North American Craton, *Geophys. Res. Lett.*, *23*(13), 1593–1596, doi:10.1029/96GL00972.

Bostock, M. G., D. W. Eaton, and D. B. Snyder (2010), Teleseismic studies of the Canadian landmass: Lithoprobe and its legacy, *Can. J. Earth Sci.*, *47*(4), 445–461.

Broomhead, D. S., and G. P. King (1986), Extracting qualitative dynamics from experimental data, *Phsica D.*, *20*, 217–236.

Bunge, H.-P., and S. Grand (2000), Mesozoic plate-motion history below the northeast Pacific Ocean from seismic images of the subducted Farallon slab, *Nature*, *405*, 337–340.
Cadzow, J. A. (1988), Signal enhancement—A composite property mapping algorithm, *IEEE Trans. Acoust. Speech Signal Process.*, *36*(1), 29–62.
Cassidy, J. F. (1992), Numerical experiments in broadband receiver function analysis, *Bull. Seimol. Soc. Am.*, *82*(3), 1453–1474.
Cassidy, J. F. (1995), A comparison of the receiver structure beneath stations of the Canadian National Seismograph Network, *Can. J. Earth Sci.*, *32*(7), 938–951, doi:10.1139/e95-079.
Chambers, K., J. H. Woodhouse, and A. Deuss (2005), Topography of the 410-km discontinuity from *PP* and *SS* precursors, *Earth Planet. Sci. Lett.*, *235*, 610–622.
Clowes, R. M., M. J. A. Burianyk, A. R. Gorman, and E. R. Kanasewich (2002), Crustal velocity structure from SAREX, the Southern Alberta Refraction Experiment, *Can. J. Earth Sci.*, *39*, doi:10.1139/E01-070.
Contenti, S. M., Y. J. Gu, A. Okeler, and M. D. Sacchi (2012), Shear wave reflectivity imaging of the Nazca-South America subduction zone: Stagnant slab in the mantle transition zone?, *Geophys. Res. Lett.*, *39*, L02310, doi:10.1029/2011GL050064.
Courtier, A. M., and J. Revenaugh (2007), Deep upper-mantle melting beneath the Tasman and Coral Seas detected with multiple ScS reverberations, *Earth Planet. Sci. Lett.*, *259*(1), 66–76.
Courtier, A. M., J. Revenaugh, M. G. Bostock, J. B. Gaherty, and E. J. Garnero (2006), Upper mantle discontinuity structure from receiver functions along the CANOE array, Abstract S41E-03 presented at 2006 Fall Meeting, AGU, San Francisco, Calif.
Crotwell, H. P., and T. J. Owens (2005), Automated receiver function processing, *Seismol. Res. Lett.*, *76*(6), 702–709.
Currie, C. A., and R. D. Hyndman (2006), The thermal structure of subduction zone back arcs, *J. Geophys. Res.*, *111*, B08404, doi:10.1029/2005JB004024.
Dalton, C. A., J. B. Gaherty, and A. M. Courtier (2011), Crustal vs structure in northwestern Canada: Imaging the Cordillera-craton transition with ambient noise tomography, *J. Geophys. Res.*, *116*, B12315, doi:10.1029/2011JB008499.
Deuss, A. (2009), Global observations of mantle discontinuities using *SS* and *PP* precursors, *Surv. Geophys.*, *30*, 301–326, doi:10.1007/s10712-009-9078-y.
Deuss, A., and J. H. Woodhouse (2002), A systematic search for mantle discontinuities using *SS*-precursors, *Geophys. Res. Lett.*, *29* (8), 1249, doi:10.1029/2002GL014768.
Dziewonski, A. M., and D. L. Anderson (1981), Preliminary reference Earth model, *Phys. Earth Planet. Int.*, *25*(4), 297–356, doi:10.1016/0031-9201(81)90046-7.
Eaton, D. W., and J. F. Cassidy (1996), A relic Proterozoic subduction zone in western Canada: New evidence from seismic reflection and receiver function data, *Geophys. Res. Lett.*, *23*(25), 3791–3794, doi:10.1029/96GL03619.
Flanagan, M. P., and P. M. Shearer (1998), Global mapping of topography on transition zone velocity discontinuities by stacking *SS* precursors, *J. Geophys. Res.*, *103*(B2), 2673–2692, doi:10.1029/97JB03212.
Flanagan, M. P., and P. M. Shearer (1999), A map of topography on the 410-km discontinuity from *PP* precursors, *Geophys. Res. Lett.*, *26*(5), 549–552.
Frederiksen, A. W., M. G. Bostock, and J. F. Cassidy (2001), *S*-wave velocity structure of the Canadian upper mantle, *Phys. Earth. Planet. Int.*, *124*, 175–191.
Ghil, M., and R. Vautard (1991), Interdecadal oscillations and the warming trend in global temperature time series, *Nature*, *350*, 324–327.
Golub, G. H., and C. F. Van Loan (1989), *Matrix Computations*, 2nd ed., Johns Hopkins University Press, Baltimore, Md.
Gorman, A. R., et al. (2002), Deep probe: Imaging the roots of western North America, *Can. J. Earth Sci.*, *39*, doi:10.1139/E01-064.
Grand, S. P. (1994), Mantle shear structure beneath the Americas and surrounding oceans, *J. Geophys. Res.*, *99*(B6), 11,591–11,621, doi:10.1029/94JB00042.
Grand, S. P. (2002), Mantle shear-wave tomography and the fate of subducted slabs, *Philos. Trans. R. Soc. London, Ser. A*, *360*(1800), 2475–2491.
Grand, S. P., and D. V. Helmberger (1984), Upper mantle shear structure of North America, *Geophys. J. R. Astron. Soc.*, *76*(2), 399–438, doi:10.1111/j.1365-246X.1984.tb05053.x.
Grand, S. P., R. D. van der Hilst, and S. Widiyantoro (1997), Global seismic tomography: A snapshot of convection in the Earth, *GSA Today.*, *7*(4), 2–7.
Gu, Y. J., and A. M. Dziewonski (2002), Global variability of transition zone thickness, *J. Geophys. Res.*, *107*(B7), 2135, doi:10.1029/2001JB000489.
Gu, Y. J., and M. D. Sacchi (2009), Radon transform methods and their applications in mapping mantle reflectivity structure, *Surv. Geophys.*, *30*, 327–354, doi:10.1007/s10712-009-9076-0.
Gu, Y. J., A. M. Dziewonski, and C. B. Agee (1998), Global de-correlation of the topography of transition zone discontinuities, *Earth Planet. Sci. Lett.*, *157*(1–2), 57–67, doi:10.1016/S0012-821X(98)00027-2.
Gu, Y. J., A. M. Dziewonski, and G. Ekström (2003), Simultaneous inversion for mantle shear velocity and topography of transition zone discontinuities, *Geophys. J. Int.*, *154*, 559–583.
Gu, Y. J., A. Okeler, L. Shen, and S. Contenti (2011), The Canadian Rockies and Alberta Network (CRANE): New constraints on the Rockies and Western Canada Sedimentary Basin, *Seismol. Res. Lett.*, *82*(4), doi:10.1785/gssrl.82.4.575.
Gu, Y. J., A. Okeler, and R. Schultz (2012), Tracking slabs beneath northwestern Pacific subduction zones, *Earth Planet. Sci. Lett.*, doi:10.1016/j.epsl.2012.03.023.
Helffrich, G. (2000), Topography of the transition zone seismic discontinuities, *Rev. Geophys.*, *38*, 141–158.
Hoffman, P. F. (1988), United plates of America, The birth of a Craton: Early Proterozoic assembly and growth of Laurentia, *Annu. Rev. Earth Planet. Sci.*, *16*, 543–603, doi:10.1146/annurev.earth.16.1.543.
Houser, C., and Q. Williams (2010), Reconciling Pacific 410 and 660km discontinuity topography, transition zone shear velocity patterns, and mantle phase transitions, *Earth Planet. Sci. Lett.*, *296*(3), 255–266.
Houser, C., G. Masters, M. Flanagan, and P. Shearer (2008), Determination and analysis of long-wavelength transition zone structure using *SS* precursors, *Geophys. J. Int.*, *174*(1), 178–194, doi:10.1111/j.1365-246X.2008.03719.x.
Huang, J., and D. Zhao (2006), High-resolution mantle tomography of China and surrounding regions, *J. Geophys. Res.*, *111*, B09305, doi:10.1029/2005JB004066.
Ita, J., and L. Stixrude (1992), Petrology, elasticity, and composition of the mantle transition zone, *J. Geophys. Res.*, *97*(B5), 6849–6866, doi:10.1029/92JB00068.
Jasbinsek, J., and K. G. Dueker (2007), Ubiquitous low-velocity layer atop the 410-km discontinuity in the northern Rocky Mountains, *Geochem. Geophys. Geosyst.*, *8*, Q10004, doi:10.1029/2007GC001661.
Katsura, T., and E. Ito (1989), The system Mg_2SiO_4-Fe_2SiO_4 at high pressures and temperatures: Precise determination of stabilities of olivine, modified spinel, and spinel, *J. Geophys. Res*, *94*(B11), 15,663–15,670, doi:10.1029/JB094iB11p15663.

Katsura, T., et al. (2004), Olivine-wadsleyite transition in the system $(Mg,Fe)_2SiO_4$, *J. Geophys. Res.*, *109*, B02209, doi:10.1029/2003JB002438.
Kennett, B. L. N., and E. R. Engdahl (1991), Traveltimes for global earthquake location and phase identification, *Geophys. J. Int.*, *105*(2), 429–465.
Langston, C. A. (1977), Corvallis, oregon, crustal and upper mantle receiver structure from teleseismic *P* and *S* waves, *Bull. Seismol. Soc. Am.*, *67*(3), 713–724.
Langston, C. A. (1979), Structure under Mount Rainier, Washington, inferred from teleseismic body waves, *J. Geophys. Res.*, *84*(B9), 4749–4762, doi:10.1029/JB084iB09p04749.
Lawrence, J. F., and P. M. Shearer (2006), A global study of transition zone thickness using receiver functions, *J. Geophys. Res.*, *111*, B06307, doi:10.1029/2005JB003973.
Lawrence, J. F., and P. M. Shearer (2008), Imaging mantle transition zone thickness with *SdS-SS* finite-frequency sensitivity kernels, *Geophys. J. Int.*, *174*(1), 143–158, doi:10.1111/j.1365-246X.2007.03673.x.
Levander, A., C. A. Zelt, and Magnani M. B. (2005), Crust and upper mantle velocity structure of the southern Rocky Mountains from the Jemez Lineament to the Cheyenne Belt, in *The Rocky Mountain Region: An Evolving Lithosphere Tectonics, Geochemistry, and Geophysics*, pp. 293–308, AGU, Washington, D. C., doi:10.1029/154GM22.
Li, X. D., and B. Romanowicz (1996), Global mantle shear velocity model developed using nonlinear asymptotic coupling theory, *J. Geophys. Res.*, *101*(B10), 22,245–22,273, doi:10.1029/96JB01306.
Ligorria, J. P., and C. J. Ammon (1999), Iterative deconvolution and receiver-function estimation, *Bull. Seismol. Soc. Am.*, *89*(5), 1395–1400.
Liu, K. H., S. S. Gao, P. G. Silver, and Y. Zhang (2003), Mantle layering across central South America, *J. Geophys. Res.*, *108*(B11), 2510, doi:10.1029/2002JB002208.
Liu, Q., and Y. J. Gu (2012), Seismic imaging: From classical to adjoint tomography, *Tectonophysics*, doi:10.1016/j.tecto.2012.07.006.
Melbourne, T. I., and D. V. Helmberger (2002), Whole mantle shear structure beneath the East Pacific Rise, *J. Geophys. Res.*, *107*(B9), 2204, doi:10.1029/2001JB000332.
Mercier, J. P., M. G. Bostock, P. Audet, J. B. Gaherty, E. J. Garnero, and J. Revenaugh (2008), The teleseismic signature of fossil subduction: Northwestern Canada, *J. Geophys. Res.*, *113*, B04308, doi:10.1029/2007JB005127.
Mercier, J. P., M. G. Bostock, J. F. Cassidy, K. Dueker, J. B. Gaherty, E. J. Garnero, J. Revenaugh, and G. Zandt (2009), Body-wave tomography of western Canada, *Tectonophysics*, doi:10.1016/j.tecto.2009.05.030.
Montelli, R., G. Nolet, F. A. Dahlen, G. Masters, E. R. Engdahl, and S. Hung (2004), Finite-frequency tomography reveals a variety of plumes in the mantle, *Science*, *303*(5656), 338–343, doi:10.1126/science.1092485.
Neele, F., H. de Regt, and J. VanDecar (1997), Gross errors in upper-mantle discontinuity topography from underside reflection data, *Geophys. J. Int.*, *129*, 194–204.
Nettles, M., and A. Dziewonski (2008), Radially anisotropic shear velocity structure of the upper mantle globally and beneath North America, *J. Geophys. Res.*, *113*, B02303, doi:10.1029/2006JB004819.
Obayashi, M., H. Sugioka, J. Yoshimitsu, and Y. Fukao (2006), High temperature anomalies oceanward of subducting slabs at the 410-km discontinuity, *Earth Planet. Sci. Lett.*, *243*(1–2), 149–158, doi:10.1016/j.epsl.2005.12.032.
Oropeza, V., and M. D. Sacchi (2011), Simultaneous seismic de-noising and reconstruction via Multichannel Singular Spectrum Analysis (MSSA), *Geophysics*, *76*(3), doi:10.1190/1.3552706.
Press, W. H., B. P. Flannery, S. A. Teukolsky, and W. T. Veterling (1992), *Numerical Recipes in FORTRAN: The Art of Scientific Computing*, 2nd ed., Cambridge Univ. Press, Cambridge, U. K.
Rigden, S. M., G. D. Gwanmesia, J. D. F. Gerald, I. Jackson, and R. C. Liebermann (1991), Spinel elasticity and seismic structure of the transition zone of the mantle, *Nature*, *354*, 143–145.
Ritsema, J., H. J. van Heijst, and J. H. Woodhouse (2004), Global transition zone tomography, *J. Geophys. Res.*, *109*, B02302, doi:10.1029/2003JB002610.
Rondenay, S. (2009), Upper mantle imaging with array recordings of converted and scattered teleseismic waves, *Surv. Geophys.*, *30*, 377–405, doi:10.1007/s10712-009-9071-5.
Ross, G. M. (2002), Evolution of Precambrian continental lithosphere in Western Canada: Results from Lithoprobe studies in Alberta and beyond, *Can. J. Earth Sci.*, *39*, doi:10.1139/E02-012.
Ross, G. M., and D. W. Eaton (2002), Proterozoic tectonic accretion and growth of western Laurentia: Results from Lithoprobe studies in northern Alberta, *Can. J. Earth Sci.*, *39*, doi:10.1139/E01-081.
Ross, G. M., R. R. Parrish, M. E. Villeneuve, and S. A. Bowring (1991), Geophysics and geochronology of the crystalline basement of the Alberta Basin, western Canada, *Can. J. Earth Sci.*, *28*(4), doi:10.1139/e91-045.
Rost, S., and C. Thomas (2009), Improving seismic resolution through array processing techniques, *Surv. Geophys.*, *30*, 271–299, doi:10.1007/s10712-009-9070-6.
Sacchi, M. D. (1997), Re-weighting strategies in seismic deconvolution, *Geophys. J. Int.*, *129*, 651–656, doi:10.1111/j.1365-246X.1997.tb04500.x.
Sacchi, M. D., and T. J. Ulrych (1995), High resolution velocity gathers and offset space reconstruction, *Geophysics*, *60*, 1169–1177.
Schaeffer, A. J., and M. G. Bostock (2010), A low-velocity zone atop the transition zone in northwestern Canada, *J. Geophys. Res.*, *115*, B06302, doi:10.1029/2009JB006856.
Schmandt, B., K. G. Dueker, S. Hansen, Jasbinsek, J. J., and Z. Zhang (2011), A sporadic low-velocity layer atop the western U.S. mantle transition zone and short-wavelength variations in transition zone discontinuities, *Geochem. Geophys. Geosyst.*, *12*, Q08014, doi:10.1029/2011GC003668.
Schmandt, B., K. G. Dueker, E. Humphreys, and S. Hansen (2012), Hot mantle upwelling across the 660 beneath Yellowstone, *Earth Planet. Sci. Lett.*, *331–332*, 224–236, doi:10.1016/j.epsl.2012.03.025.
Schmerr, N., and E. J. Garnero (2007), Upper mantle discontinuity topography from thermal and chemical heterogeneity, *Science*, *318*(5850), 623–626, doi:10.1126/science.1145962.
Schmid, C., S. Goes, S. van der Lee, and D. Giardini (2002), Fate of the Cenozoic Farallon slab from a comparison of kinematic thermal modeling with tomographic images, *Earth Planet. Sci. Lett.*, doi:10.1016/S0012-821X(02)00985-8.
Schoellhamer, D. H. (2001), Singular spectrum analysis for time series with missing data, *Geophys. Res. Lett.*, *28*, 3187–3190, doi:10.1029/2000GL012698.
Schultz, R., and Y. J. Gu (2013), Flexible, inversion-based MATLAB implementation of the Radon transform, *Comput. Geosci.*, *52*, 437–442.
Sears, J. W., T. A. Harms, and C. A. Evenchick (2007), Whence the mountains? The contributions of Raymond A. Price, *Geol. Soc. Am. Spec. Pap.*, *433*, xi–xviii.
Shearer, P. M. (1991), Constraints on upper mantle discontinuities from observations of long-period reflected and converted phases, *J. Geophys. Res.*, *96*(B11), 18,147–18,182, doi:10.1029/91JB01592.
Shearer, P. M., and G. T. Masters (1992), Global mapping of topography on the 660-km discontinuity, *Nature*, *355*, 791–796.

Shragge, J., M. G. Bostock, C. G. Bank, and R. M. Ellis (2002), Integrated teleseismic studies of the southern Alberta upper mantle, *Can. J. Earth Sci.*, *39*(3), 399–411, doi:10.1139/e01-084.

Simmons, N. A., A. M. Forte, L. Boschi, and S. P. Grand (2010), GyPSuM: A joint tomographic model of mantle density and seismic wave speeds, *J. Geophys. Res.*, *115*, B12310, doi:10.1029/2010JB007631.

Takens, F. (1981), Detecting strange attractors in turbulence, *Lect. Notes Math.*, *898*, 366–381.

Tauzin, B., E. Debayle, and G. Wittlinger (2008), The mantle transition zone as seen by global *Pds* phases: No clear evidence for a thin transition zone beneath continents, *J. Geophys. Res.*, *113*, B08309, doi:10.1029/2007JB005364.

Tauzin, B., E. Debayle, and G. Wittlinger (2010), Seismic evidence for a global low-velocity layer within the Earth's upper mantle, *Nat. Geosci.*, *3*(10), 718–721, doi:10.1038/ngeo969.

Thompson, D. A., G. Helffrich, I. D. Bastow, J. M. Kendall, J. Wookley, D. W. Eaton, and D. B. Snyder (2011), Implications of a simple mantle transition zone beneath cratonic North America, *Earth Planet. Sci. Lett.*, doi:10.1016/j.epsl.2011.09.037.

Trickett, S. R. (2003), F-xy eigenimage noise suppression, *Geophysics*, *68*(2), 751–759.

van der Lee, S., and G. Nolet (1997), Upper mantle *S* velocity structure of North America, *J. Geophys. Res.*, *102*(B10), 22,815–22,838, doi:10.1029/97JB01168.

van der Meijde, M., F. Marone, D. Giardini, and S. van der Lee (2003), Seismic evidence for water deep in Earth's upper mantle, *Science*, *300*(5625), 1556–1558.

van der Meijde, M., S. van der Lee, and D. Giardini (2005), Seismic discontinuities in the Mediterranean mantle, *Phys. Earth Planet. Int.*, *148*(2–4), 233–250, doi:10.1016/j.pepi.2004.09.008.

Vinnik, L. P. (1977), Detection of waves converted from *P* to *SV* in the mantle, *Phys. Earth Planet. Inter.*, *15*, 39–45.

Weidner, D. J., and Y. Wang (1998), Chemical- and Clapeyron-induced buoyancy at the 660 km discontinuity, *J. Geophys. Res.*, *103*(B4), 7431–7441, doi:10.1029/97JB03511.

Wessel, P., and W. H. F. Smith (1998), New improved version of the Generic Mapping Tools released, *Eos Trans. AGU*, *79*, 579, doi:10.1029/98EO00426.

Zhao, D. (2001), Seismological structure of the subduction zones and its implication for arc magmatism and dynamics, *Phys. Earth Planet. Inter.*, *127*, 197–214.

Zhao, D. (2004), Global tomographci images of mantle plumes and subducting slabs: Insight into deep Earth dynamics, *Phys. Earth Planet. Inter.*, *146*, 3–34.

Zheng, Y., T. Lay, M. P. Flanagan, and Q. Williams (2007), Pervasive seismic wave reflectivity and metasomatism of the Tonga mantle wedge, *Science*, *316*(855), doi:10.1126/science.1138074.

Zhou, Y., F. Dahlen, and G. Nolet (2004), Three-dimensional sensitivity kernels for surface wave observables, *Geophys. J. Int.*, *158*, 142–168.

Zhu, L., and H. Kanamori (2000), Moho depth variation in southern California from teleseismic receiver functions, *J. Geophys. Res.*, *105*(B2), 2969–2980, doi:10.1029/1999JB900322.